



Binary sulfuric effect on ZnO laminated carbon nanofibers hybrid structure for ultrafast lithium storage capability

Kue-Ho Kim^a, Weiguang Hu^b, Hyo Sik Chang^{b,*}, Hyo-Jin Ahn^{a,*}

^a Department of Materials Science and Engineering, Seoul National University of Science and Technology, Seoul 01811, South Korea

^b Graduate School of Energy Science & Technology, Chungnam National University, 34134, South Korea



ARTICLE INFO

Article history:

Received 1 September 2021

Received in revised form 22 November 2021

Accepted 4 December 2021

Available online 7 December 2021

Keywords:

Li-ion battery

Ultrafast Li-ion storage

Laminated hybrid structure

Zinc oxide

Carbon nanofibers

ABSTRACT

The hybrid structure of high conductive carbon materials with large capacitive metal compounds is one of promising strategies for achieving high specific capacity, cycling stability, and ultrafast Li-ion storage capability due to their synergistic effects. This article will demonstrate the novel hybrid structure of a zinc oxysulfide (ZnOS) lamination layer on a sulfur (S)-doped carbon nanofiber (SCNF) matrix via an electrospinning method with sequential atomic layer deposition (ALD) process and will also present the structural advantages for ultrafast Li-ion batteries (LIBs). As a double-anion material, ZnOS has benefits compared with single ZnO and ZnS during the charge/discharge process, which is accompanied with consecutive conversion and alloying reactions. To verify these factors, structural analysis at the atomic scale and various electrochemical properties were evaluated. The resultant ZnOS/SCNF electrode showed superior electrochemical performance such as high specific capacity (672.8 mAh g^{-1} at 100 mA g^{-1}), good capacity retention (87.8% after 100 cycles), and excellent cycling stability (85.4% after 500 cycles). This is attributed to the facilitated kinetic properties including electron and ion transfer efficiency during the electrochemical reactions, accompanied with the ZnOS/SCNF hybrid structure. In this regards, we believe that the ZnOS/SCNF electrode could be a great reference as a promising research strategy for accomplishing ultrafast LIBs.

© 2021 Elsevier B.V. All rights reserved.

1. Introduction

In accordance with the rising global energy demand, lithium ion batteries (LIBs) are becoming increasingly in demand as an ubiquitous energy storage medium for portable electronics, electric vehicles, and a variety of other devices (e.g., power tools, drones, and satellites) [1–3]. The technology associated with LIBs have been developing rapidly, starting from the 1990 s, and most of the initial research strategies were focused on enhancing the specific capacity or cycle stability. But these days, as LIBs have been adopted by a wide application of fields, the specific needs of customers have become very important, such as high-rate capability, high sustainability, fire stability and affordable cost. Since the exploding electric vehicle market has brought unprecedented demand for LIBs, naturally, the further development of LIB technology is required. Among market issues, improving fast energy storage capability is one of the key technologies to break the

limitation of the current energy storage system with LIBs. Since the performance of LIBs predominantly depends on the electrochemical characteristics of anode and cathode materials, various research strategies were suggested such as doping, coating, and composite [4,5]. Among them, constructing hybrid structures is known as a powerful strategy for performance enhancement. Especially at the anode, widely used graphite often presents limitations of low theoretical capacity (372 mA h g^{-1}) and insufficient intercalation kinetics at a high current density, which makes it no longer able to fulfill the increasing market demand [6,7].

In the last few years, several transition metal oxide materials have been suggested as potential anode materials for LIBs such as SnO_2 , MnO , Co_3O_4 , and ZnO due to their high theoretical capacities, low cost, and a simple synthesis methods [8–11]. Among these materials, ZnO has been nominated as a great potential material as an anode in LIBs due to its high theoretical specific capacity of 978 mA h g^{-1} , abundance on Earth, and both thermal and chemical stability. However, using pure ZnO as an anode material causes critical problems by its volume expansion and low conductivity characteristics. During the charging process, ZnO reduces into metallic Zn and Li_xZn alloy with Li-ion intercalation, which leads to severe volume expansion and loss of active material. Moreover, the low

* Corresponding authors.

E-mail addresses: hschang@cnu.ac.kr (H.S. Chang), hjahn@seoultech.ac.kr (H.-J. Ahn).

conductivity of ZnO limits the electrochemical reaction kinetics especially at the high current density, provoking poor high-rate performance of LIBs. Likewise, transition metal sulfides (SnS, WS₂, ZnS, etc.) also have been studied as promising anode materials owing to their unique characteristics compared with transition metal oxides [12–14]. For example, ZnS possesses higher conductivity than ZnO while the theoretical specific capacity (962.3 mA h g⁻¹) is slightly lower. Furthermore, ZnS suffers from its insufficient electrical conductivity and volume expansion issues at high current density when used alone. To achieve superior high-rate performance with long cycle stability as well as to overcome these limitations, two different strategies have been mainly adopted. The first one is decreasing the size or layer thickness of the metal compounds to avoid drastic volume expansion and shorten the Li-ion diffusion pathway. For example, Li et al. reported the electrode fabricated with highly dispersed ZnO nanoparticles using scalable sol-gel synthetic technique, which showed 229 mA h g⁻¹ at a high current density of 1.5 C (~1500 mA g⁻¹) [15]. The second strategy is to construct a hybrid structure with high-conductive materials. Carbon-based materials are often utilized as a composite element due to their high conductivity, electrochemical stability, and low cost. This hybrid structure with carbon materials can offer high electrical conductivity and reduce volume expansion effectively, which enables superior high-rate performance and long cycle stability of LIBs. However, despite these efforts, it has proved difficult to achieve excellent high-rate performance and good long-cycle stability simultaneously. In addition, the hybrid structure of zinc oxy-sulfide (ZnOS) with carbon matrix for improving high-rate performance and cycle stability has not been reported to date.

In this study, we will first report a novel hybrid structure of ZnOS lamination layer on sulfur (S)-doped carbon nanofibers (ZnOS/SCNF) using a sequential atomic layer deposition (ALD) for ultrafast anode materials in LIBs. During the ALD process, a ZnO and ZnS layer was deposited according to the fixed composition sequentially and sulfur was successfully doped within CNF matrix. The laminated ZnOS layer with S-doped CNF matrix enables stable and ultrafast Li-ion storage capability. Compared with ZnO/CNF and ZnS/SCNF, the ZnOS/SCNF showed excellent specific capacity at both low and high current density with high stability up to 500 cycles.

2. Experimental details

2.1. Preparation of the CNFs

As a framework of ZnOS/SCNF, CNFs were fabricated using electrospinning method, followed by carbonization process. To prepare a precursor solution of electrospinning process, 10 wt% polyacrylonitrile (PAN, M_w = 150,000 g mol⁻¹, Aldrich) was dissolved in N,N-dimethylformamide (DMF, 99.8%, Aldrich) and stirred for 24 h. Then, the prepared solution was placed into a 10 mL syringe with a 23 gauge needle and connected to the syringe pump. During the electrospinning process, feeding rate, needle/collector gap, and voltage were maintained at 0.03 mL h⁻¹, 15 cm, and 13 kV, respectively. As-spun PAN-based nanofibers on the Al collector were collected and carbonized at 800°C nitrogen atmosphere for 2 h after stabilizing at 280°C in air. The resultant CNFs were set aside for further ALD process.

2.2. ALD coating process

Due to several advantages of ALD, such as precise thickness control, large area uniformity, and highly conformal deposition, we employed the thermal ALD technique to deposit a ZnO, ZnS, and ZnOS lamination layer onto the as-prepared CNF. All ALD deposition temperatures were 140°C. During the ZnO ALD process, conventional diethylzinc [Zn(C₂H₅)₂, or DEZn] and H₂O have been used as zinc and

oxygen precursors, respectively. Precursors are delivered from bubblers, using nitrogen as a carrier gas, and transported to the reactor through heated lines, to prevent condensation. The DEZn and H₂O bubblers are controlled by the Peltier device at 12°C and 15°C, respectively. The cycles of DEZn and H₂O exposure were 125. The ZnS ALD process and cycle are the same as the ZnO ALD process, but sulfur precursors were used instead of oxygen precursors. The ZnS layer was deposited using DEZn and H₂S gas reactants as precursors. The ZnOS lamination layer was deposited by the number of sub-cycles, which is an alternating cycle method of ZnO and ZnS. The combination of ZnO and ZnS were grown using nine cycles of ZnS ALD followed by a one cycle of ZnO ALD.

2.3. Characterizations

The structural properties and surface morphology of all the samples were investigated by field-emission scanning electron microscopy (FESEM, Hitachi SU-8010) and high-resolution transmission electron microscopy (HRTEM, JEOL JEM-2100F) inclusive of energy-dispersive spectroscopy (EDS) mapping. To characterize the thermal decomposition behavior, thermogravimetric analysis (TGA) and differential thermal analysis (DTA) were conducted up to 800°C at a heating rate of 10°C min⁻¹. The crystallographic and chemical bonding states were analyzed using X-ray diffraction measurement (XRD, Rigaku D/Max-2500) with Cu K α radiation and X-ray photoelectron spectroscopy (XPS, ESCALAB 250) with Al K α radiation. To investigate the electrochemical performance, an anode was fabricated with all prepared samples. For preparing the slurries, the weight ratio of active material: conductive material (ketjen black): binder (PVDF) was 7:1:2 with an N-methyl-2-pyrrolidinone solvent. The prepared slurries were coated on the copper foil current collector using doctor blade method and then dried in an oven for 10 h at 100°C. To compare the accurate electrochemical performances, the loading mass of active materials for all the samples were fixed to ~2 mg. Coin-type cells (CR2032, Hohsen Corp.) were assembled with 1.6 M LiPF₆ in a mixture of dimethyl carbonate and ethylene carbonate (3:7) as an electrolyte, prepared electrodes as an anode, Li metal foil (Honjo Chemical Corp., 99.999%) as the counter electrode, and a porous polypropylene membrane (Celgard 2400) as a separator. To analyze the electrochemical kinetics, electrochemical impedance spectroscopy (EIS) measurements at an open-circuit potential were performed in the frequency range of 10⁵–10⁻² Hz. The electrochemical characteristics and charge/discharge performances were examined using a battery cycler system (WonATech Corp., WMPG 3000) in the potential range of 0.05–3.0 V (vs. Li/Li⁺). The cycling stability up to 100 cycles was investigated at a current density of 100 mA g⁻¹ and rate capability was analyzed at a current density of 100, 300, 700, 1000, 1500, and 2000 mA g⁻¹. Moreover, the ultrafast cycling stability was evaluated at a high current density of 2000 mA g⁻¹ up to 500 cycles.

3. Results and discussion

Fig. 1a depicts a brief scheme of the experiment procedure to construct the ZnOS/SCNF hybrid structure. After carbonizing as-spun PAN based nanofibers, the coating layer sequentially laminated by ZnO, ZnS, and ZnOS, respectively up to 130 cycles using ALD process with different chemicals. Fig. 1b–d show the resultant structure of hybrid sample including ZnO/CNF, ZnS/SCNF, and ZnOS/SCNF, which can effectively complement the low specific capacity of CNF and low electrical conductivity of metal compounds. For confirming the weight ratio of the CNF matrix and the laminating layer, TGA measurements of all the samples were performed (see Fig. S1). From 25 to 100 °C, a slight weight loss, caused by water evaporation within CNF was frequently observed. In succession, a drastic weight loss was confirmed in the region about 450–600 °C, which was attributed

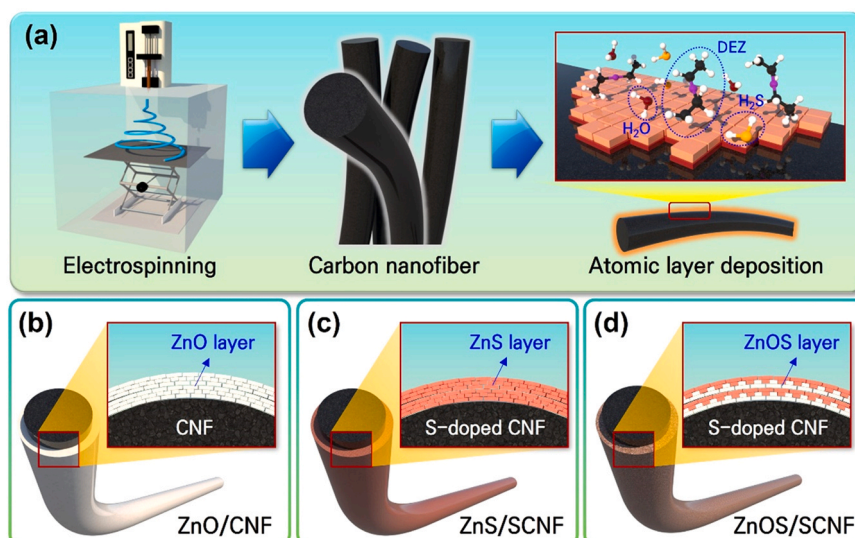


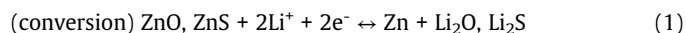
Fig. 1. (a) Schematic illustration of the synthetic procedure for novel hybrid structure of ZnOS lamination layer on SCNF matrix and (b-d) resultant structure of ZnO/CNF, ZnS/SCNF, and ZnOS/SCNF, respectively.

to the decomposition of the CNF matrix. Compared to the remaining mass (1.77%) of CNF at 800 °C, ZnO/CNF, ZnS/CNF, and ZnOS/SCNF maintained 55.2%, 49.2%, and 51.6% of total mass, which is according to the weight ratio of ZnO, ZnS, and ZnOS laminated layer.

Fig. 2a–d show the FESEM images of the CNF, ZnO/CNF, ZnS/SCNF, and ZnOS/SCNF samples, respectively. For the CNF (see Fig. 2a), a smooth surface with a diameter in the range of ~251.5–272.5 nm was observed in the one-dimensional (1D) morphology. Metal compound laminated samples also showed a similar morphology with thicker diameters (~271.5–292.5 nm for ZnO/CNF, ~292.4–315.7 nm for ZnS/SCNF, and ~289.5–310.5 nm for ZnOS/SCNF) due to the laminated layer. Also, this interconnected 1D network structure can offer effective electron and ion transfer during cycling [16]. Moreover, successful formation of core-shell hybrid structure for ZnO/CNF, ZnS/SCNF, and ZnOS/SCNF was identified without any damage to the CNF matrix during ALD process. To investigate the inner structure and

lamination thickness precisely, HRTEM analysis of surface region was conducted for all the samples (see Fig. S2). CNF showed smooth and flat carbon matrix without any coating layer. In contrast, the lamination layer was identified by dark spots due to the heavy Zn ions and the thickness was ~40.5 nm for ZnO/CNF, ~56.7 nm for ZnS/SCNF, and ~45.2 nm for ZnOS/SCNF, respectively. This varied lamination thickness despite the same ALD cycle number, is dominantly caused by the difference of a theoretical density of ZnO (5.61 g/cm³) and ZnS (4.09 g/cm³). In Fig. 3, TEM and EDS mapping images of ZnOS/SCNF were conducted for analyzing the atomic composition, which indicate a distinct distribution of C atoms at the core and homogeneously distributed Zn, O, and S atoms at the shell. The quantitative atomic percentage was summarized in Table 1 including CNF, ZnO/CNF, and ZnS/SCNF samples. ZnOS/SCNF showed atomic percentage of 73.65%, 13.37%, 11.53%, and 1.38% for the C, Zn, O, and S atoms and these results demonstrate the successful formation of ZnOS/SCNF core/shell hybrid structure as the 1D morphology. This novel hybrid structure can take both advantage of high electrical conductivity due to the 1D CNF matrix and high specific capacity and ion diffusivity of ZnOS lamination layer.

Fig. 4 shows the structural interpretation of the ZnOS lamination layer to reveal the specific factors for enhanced ultrafast Li-ion storage capability. For better understanding, the ball-stick model of a unit cell for wurtzite ZnO and zincblende ZnS structure were depicted with the lattice constant (see Fig. 4a–b). The wurtzite ZnO appears as a hexagonal feature with the space group of P6₃mc and the corresponding lattice constant (a: 3.249, b: 3.249, and c: 5.206). However, ZnS appears as a cubic feature with the space group of F4̄3m and the corresponding lattice constant (a: 5.406, b: 5.406, and c: 5.406) [17]. Since the discharging process of ZnO and ZnS firstly proceed with a conversion reaction to form Zn elements and then alloying reaction between Li and Zn, diffusion of Li-ion into the lattice structure is one of the key properties for the Li-ion storage capability (see Eq. (1–2)) [18,19].



Thus, the enlarged lattice constant with unit cell volume of zincblende ZnS compared with wurtzite ZnO is capable of providing excellent Li-ion storage performance, especially at a high current density despite the higher theoretical specific capacity of ZnO [20].

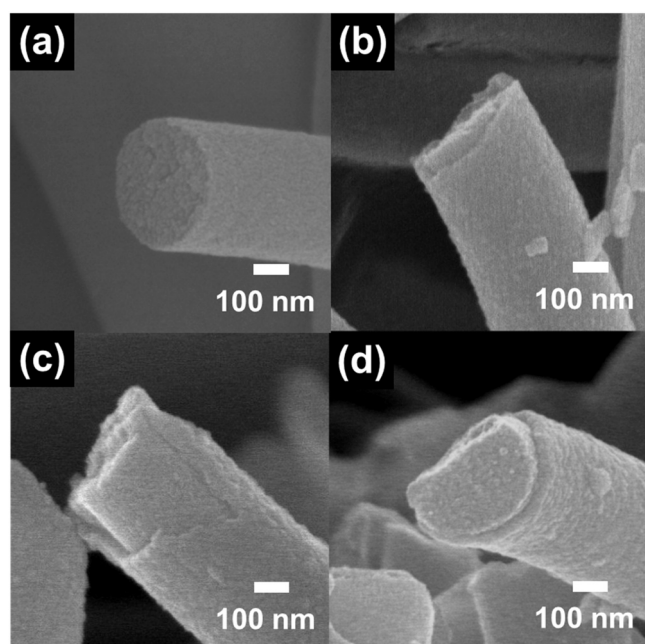


Fig. 2. FESEM images of (a) CNF, (b) ZnO/CNF, (c) ZnS/SCNF, and (d) ZnOS/SCNF.

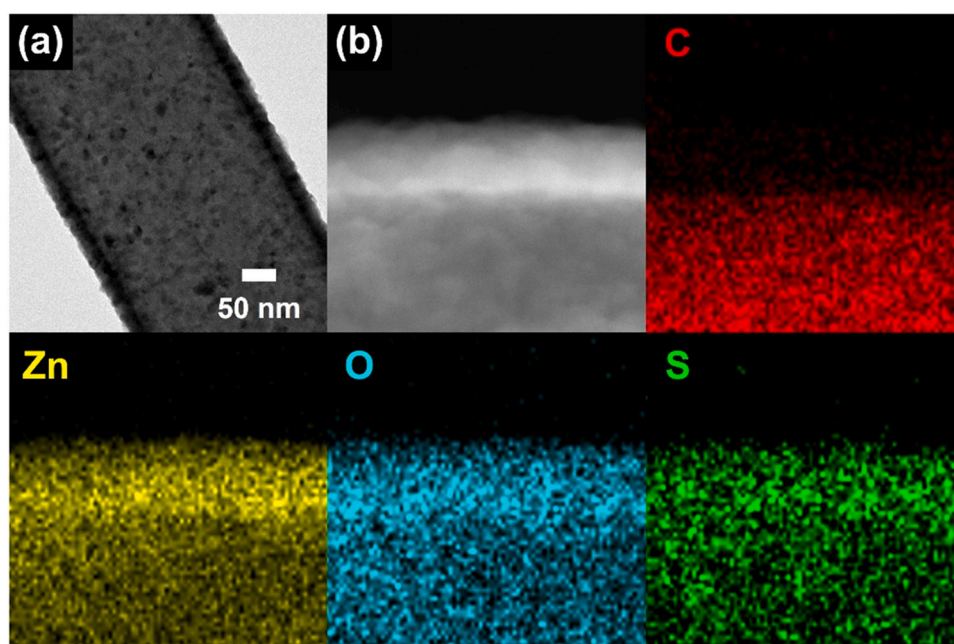


Fig. 3. (a) TEM image and (b) EDS mapping results obtained from the ZnOS/SCNF.

Table 1

Summary of quantitative atomic percentage obtained from all the samples.

Samples	C (at%)	Zn (at%)	O (at%)	S (at%)
CNF	97.85	–	2.15	–
ZnO/CNF	71.57	13.10	15.33	–
ZnS/SCNF	74.25	13.44	2.73	9.58
ZnOS/SCNF	73.65	13.37	11.53	1.38

To demonstrate this point in detail, HRTEM analysis of ZnO/CNF and ZnOS/SCNF was conducted (see Fig. S3). ZnO/CNF only shows the lattice distance of 2.6 Å, which corresponds to the (002) plane of ZnO structure. However, ZnOS/SCNF shows the two types of lattice

distances including 2.6 Å for (002) plane of ZnO and 3.2 Å for (111) plane of ZnS [21,22]. Thus, we confirmed the expanded lattice of ZnOS, which can provide the efficient Li ion transportation. In this respect, the benefits of high theoretical specific capacity and large lattice constant can be achieved by forming hybrid structure of ZnOS lamination layer as seen in Fig. 4c. This hybrid structure induces a band gap reduction between the interface of ZnO and ZnS, which enables enhanced charge transfer efficiency [23]. Moreover, the generated Li₂O and Li₂S interphase can suppress the drastic alloying process of Zn with Li, providing stable electrochemical reactions during repetitive charge/discharge processes [24]. Thus, the suggested novel ZnOS/SCNF hybrid structure achieve high electrical conductivity and stable Li-ion alloying reaction, which can realize

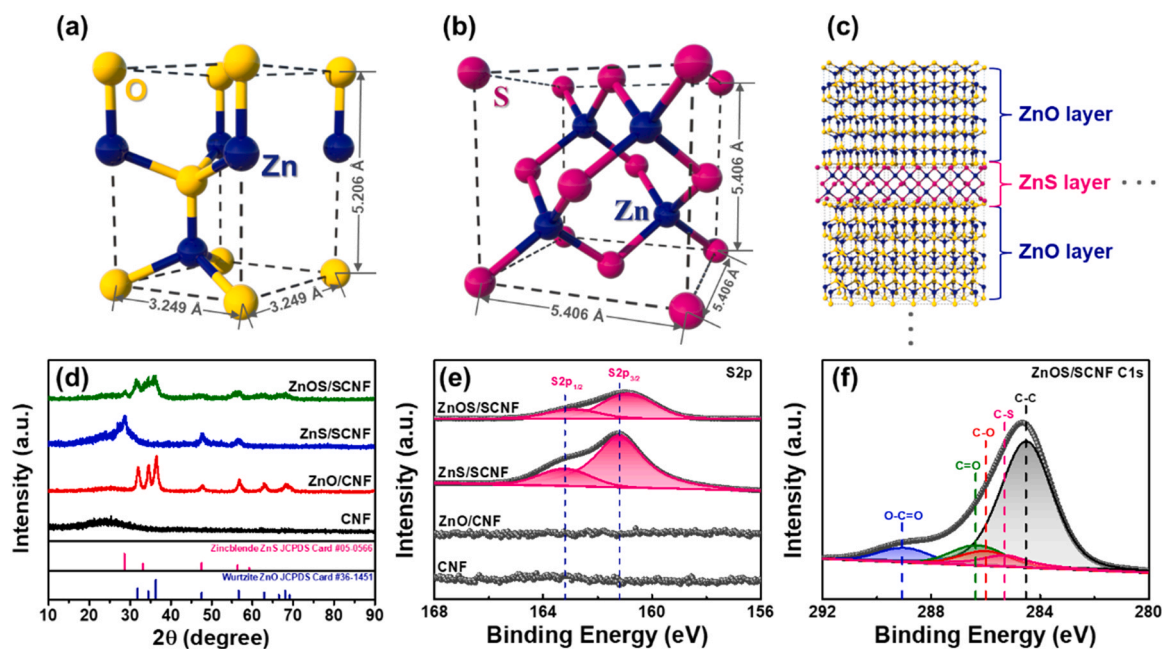


Fig. 4. (a–c) Ball-stick lattice structure model of wurtzite ZnO, ZnS, and ZnOS lamination layer, (d) XRD curves and XPS core-level spectra of (e) S 2p obtained from CNF, ZnO/CNF, ZnS/SCNF, and ZnOS/SCNF, and (f) XPS core-level spectra of C 1s for ZnOS/SCNF.

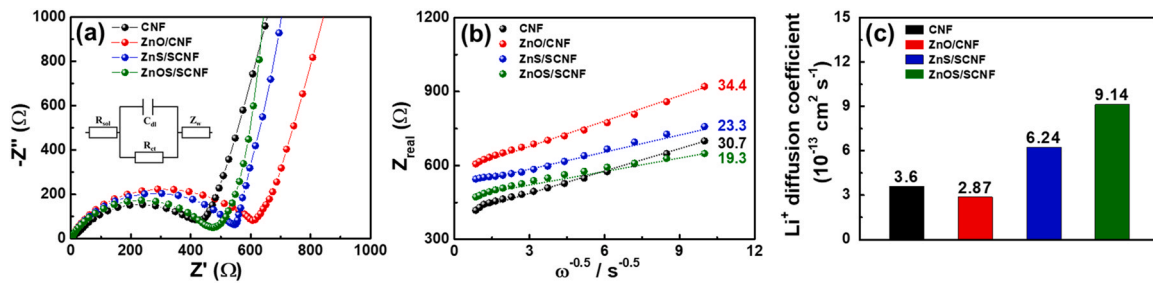


Fig. 5. (a) Nyquist plots and (b) relationship between Z_{real} and $\omega^{-0.5}/s^{-0.5}$ in the low frequency calculated by Nyquist plots, and (c) Li-ion diffusion coefficient of CNF, ZnO/CNF, ZnS/SCNF, and ZnOS/SCNF electrodes, respectively.

the superior Li-ion storage capability at high current densities and excellent cycle stability. To verify these structural properties, Fig. 4d shows the XRD curves of the CNF, ZnO/CNF, ZnS/SCNF, and ZnOS/SCNF samples. CNF only shows one broad peak at $\sim 25.00^\circ$, corresponding to the (002) plane of amorphous graphite compared with other laminated samples [25]. Otherwise, ZnO/CNF reveals characteristic peaks at 31.79° , 34.45° , 36.28° , 47.58° , 56.65° , 62.92° , and 68.02° , corresponding to the respective (100), (002), (101), (102), (110), (103), and (112) planes of wurtzite ZnO structure (JCPDS card #36-1451) [26]. In addition, characteristic peaks at 28.58° , 47.56° , and 56.34° were observed, which are corresponding to the respective (111), (220), and (311) planes of zincblende ZnS structure (JCPDS card #05-0566) [27]. This result confirm successful formation of a ZnO and ZnS structure on the CNF matrix via sequential ALD process. The weak diffraction peak of amorphous graphite, which also existed in the laminated samples, was hard to discern due to other strong characteristic peaks. Furthermore, ZnOS/SCNF dominantly exhibits the structure property of ZnO with little ZnS peaks, which is attributed to the difference in lamination sequence ratio (ZnO (9): ZnS (1)) during ALD process. To characterize the chemical bonding state, XPS measurements were conducted for all the samples (see Fig. 4e–f), which were arranged according to the 284.5 eV C1s bonding as a reference. Fig. S4 shows the Zn 2p XPS core-level spectra, demonstrating the existence of one-pair doublet at around 1044.62 eV for Zn $2p_{1/2}$ and around 1021.59 eV for Zn $2p_{3/2}$ except for the CNF sample. Interestingly, a blue shift of Zn related binding energy was observed with ZnOS/SCNF and ZnS/SCNF compared with ZnO/CNF (from 1044.62 eV and 1021.59–1044.88 eV and 1021.89 eV for ZnOS/SCNF and 1045.14 eV and 1022.24 for ZnS/SCNF). This phenomenon indicates good accordance with the lower binding energy of Zn 2p state in ZnO compared to the Zn 2p state in ZnS [28]. In Fig. 4e, two peaks were observed at the binding energies of 163.20 eV and 161.19 eV for ZnS/SCNF, which are indicative of S $2p_{1/2}$ and S $2p_{3/2}$, respectively [29]. Due to a reduced charge on the sulfur elements in the laminated sulfur-oxygen matrix, ZnOS/SCNF shows red shift (162.88 eV for S $2p_{1/2}$ and 160.89 eV for S $2p_{3/2}$) compared with the binding energy of ZnS/SCNF [30]. Moreover, Fig. 4f shows the C 1s XPS spectra of ZnOS/SCNF sample, which appears five peaks at 284.5 eV, 285.3 eV, 286 eV, 286.4, and 289.1 eV, corresponding to the binding energy of C-C, C-O, C-S, C=O, and O-C=O bonds, respectively. The C-S bond was generated during the ALD process, indicating the formation of S-doped carbon structure within CNF matrix. As the S atom in carbon lattice can offer extra electrons through spin-orbit coupling, this S-doped carbon structure is expected to increase electrical conductivity [31]. These XPS results confirm the variation of chemical bonding state of ZnOS/SCNF in comparison with ZnO/CNF and ZnS/SCNF, which indicates the successful formation of a hybrid structure.

To investigate the electrochemical kinetic properties of all the fabricated anode, EIS analyses were conducted using as-assembled coin-type cells. Fig. 5a displays the Nyquist plots of the CNF, ZnO/CNF, ZnS/SCNF, and ZnOS/SCNF. The Nyquist plots can be classified as

a single semicircle region in the high frequencies and an inclined line region in the low frequencies [32]. First, the semicircle region indicates the charge transfer resistance (R_{ct}), which is related to the interfacial resistance between anode and electrolyte. Among the laminated samples, ZnOS/SCNF show the smallest semicircle size, implying the highest electrical conductivity. Furthermore, to identify the electrical conductivity in detail, the electrical conductivity of commercial ZnO nanoparticles, CNF, ZnO/CNF, ZnS/SCNF, and ZnOS/SCNF electrodes were measured by Hall-effect measurement system (see Fig. S5). Due to the high electrical conductivity of CNF, composite electrodes show enhanced electrical conductivity (0.86 S cm^{-1} , 0.98 S cm^{-1} , and 1.10 S cm^{-1} for ZnO/CNF, ZnS/SCNF, and ZnOS/SCNF electrodes) compared with the commercial ZnO nanoparticles electrode (0.47 S cm^{-1}). This result is mainly attributed to the enhanced electron transfer efficiency between the ZnO and ZnS interface region and high electrical conductivity of S-doped CNF matrix. Second, the inclined line region is correlated with Li-ion diffusion, which is defined as Warburg impedance (see Fig. 5b). ZnOS/SCNF shows the lowest Warburg impedance, resulting from the novel hybrid structure with a favorable ion diffusion pathway due to the expanded lattice constant with distortion. Fig. 5c represents the calculated Li-ion diffusion coefficients of the CNF, ZnO/CNF, ZnS/SCNF, and ZnOS/SCNF using Eqs. (3) and (4) [33,34].

$$Z_R = \sigma_w \omega^{-1/2} + R_{ct} + R_e \quad (3)$$

$$D = (RT)^2/2A(n^2F^2C\sigma_w)^2 \quad (4)$$

In the equations, σ_w and R_e represent the Warburg impedance coefficient corresponding to the Li-ion diffusion resistance of the electrode material. And, D , R , T , and A indicate the Li-ion diffusion coefficient, ideal gas constant, temperature, and electrode area, respectively. Among all the samples, ZnOS/SCNF showed the highest Li-ion diffusion coefficient of $9.14 \times 10^{-13} \text{ cm}^2 \text{ s}^{-1}$ compared with the other electrodes ($3.60 \times 10^{-13} \text{ cm}^2 \text{ s}^{-1}$ for CNF, $2.87 \times 10^{-13} \text{ cm}^2 \text{ s}^{-1}$ for ZnO/CNF, and $6.24 \times 10^{-13} \text{ cm}^2 \text{ s}^{-1}$ for ZnS/SCNF, respectively). These results imply the hybrid ZnOS/SCNF structure possesses high electrical conductivity with fast Li-ion diffusivity, which mainly contributes to the ultrafast Li storage performance and cycling stability [35].

To demonstrate the electrochemical reactions during the charge/discharge cycling, cyclic voltammetry (CV) measurements were performed in the potential range of 0.05–3.0 V (vs. Li/Li⁺) at a scan rate of 0.1 mV s^{-1} . Fig. 6a exhibits the CV curves of ZnOS/SCNF for the first five consecutive cycles. According to the previous studies regarding Zn-based anode materials, ZnOS also goes through a conversion reaction during the reduction process to form Zn element. Therefore, an alloying reaction is proceeded from Zn to LiZn with a buffer layer of Li₂O and Li₂S. At the discharging stage of the initial cycle, the notable reduction processes were observed at $\sim 0.2 \text{ V}$ due to the reduction of ZnOS into Zn, the formation of Li-Zn alloy and a solid-electrolyte interphase (SEI) layer. For the charging stage, oxidation peaks were observed at $\sim 0.3 \text{ V}$, $\sim 0.38 \text{ V}$, $\sim 0.56 \text{ V}$, and $\sim 0.69 \text{ V}$,

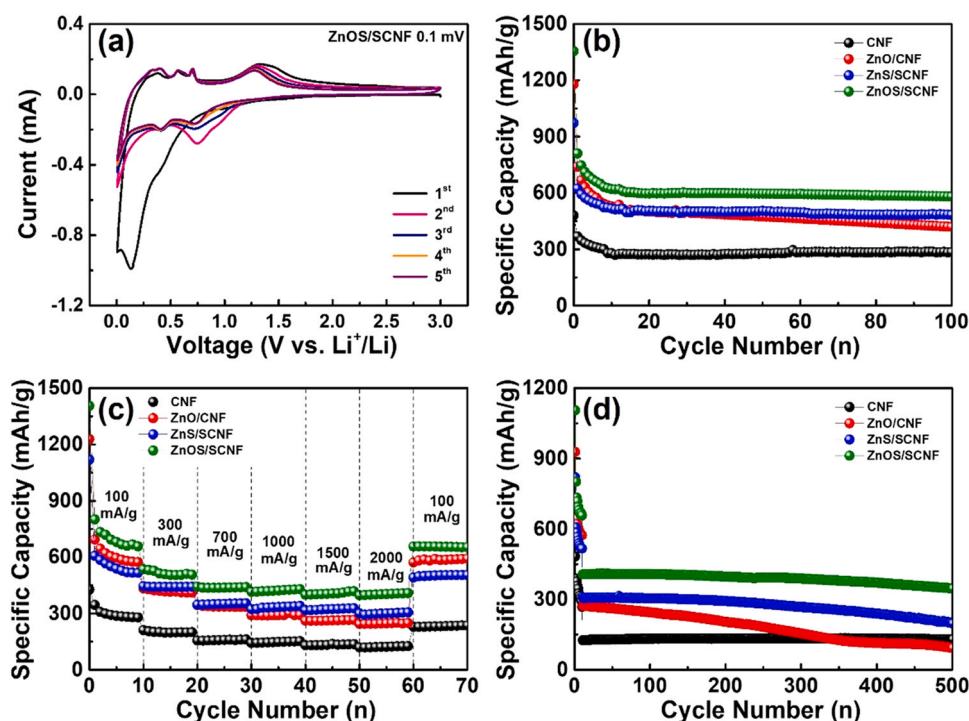


Fig. 6. (a) CV curve for the first five cycles of ZnOS/SCNF at a scan rate of 0.1 mV s⁻¹ within the potential range of 0.05–3.0 V, (b) cycling stability measurement at a current density of 100 mA g⁻¹ for 100 cycles, (c) rate performance at current densities of 100–2000 mA g⁻¹, and (d) long-term cycling test at a high current density of 2000 mA g⁻¹ up to 500 cycle of all the fabricated electrodes.

which are corresponding to the dealloying process from LiZn to Li₂Zn₃, LiZn₂, Li₂Zn₅, and LiZn₄. The broad peak at ~1.3 V indicates the regeneration of ZnOS structure from Zn, Li₂O, and Li₂S. From the second peak, the huge reduction peak disappears and new peaks appear at ~0.7 V and ~0.4 V, corresponding to the ZnOS conversion and Li-Zn alloying process [36]. Thus, the electrochemical reactions of ZnOS/SCNF electrode during the charge/discharge were well-defined and reversible CV plots were confirmed. Fig. 6b shows the cycling stability of all the electrodes obtained in the potential range of 0.05–3.0 V (vs. Li/Li⁺) at a current density of 100 mA g⁻¹ up to 100 cycles. The CNF electrode appears the lowest specific capacity of 284.6 mAh g⁻¹ at 100th cycle despite the high cycling stability due to the low theoretical specific capacity. In contrast, the metal oxide anode materials with high theoretical specific capacity such as ZnO often exhibit inferior capacity retention due to their poor electrical conductivity and excessive volume expansion [37,38]. Therefore, constructing a hybrid structure using carbon matrix and metal compounds could be a crucial strategy as suggested in this study (ZnO/CNF, ZnS/SCNF, and ZnOS/SCNF). Among them, ZnOS/SCNF shows the highest specific capacity of 584.03 mAh g⁻¹ with high capacity retention rate of 87.8% compared with the ZnO/CNF (specific capacity of 419.59 mAh g⁻¹ with 71.6% capacity retention rate) and ZnS/SCNF (specific capacity of 483.87 mAh g⁻¹ with 85.4% capacity retention rate) electrodes. The galvanostatic voltage profiles during the charging/discharging process of all the electrodes were investigated at a current density of 100 mA g⁻¹ (see Fig. S6). The initial discharge capacities were observed as 512.75 mAh g⁻¹, 1186.67 mAh g⁻¹, 983.06 mAh g⁻¹, and 1288.75 mAh g⁻¹ for CNF, ZnO/CNF, ZnS/SCNF, and ZnOS/SCNF, respectively. Specifically, the shape of voltage curves for ZnO/CNF and ZnOS/SCNF seem similar for the first few cycles, and then the rapid degradation of specific capacity was observed for ZnO/CNF, which is highly matched with the cycling stability result. This superior cycling stability at a low current density is mainly attributed to the efficient conversion and alloying reaction regarding the decomposition/reformation of ZnOS and

alloying-dealloying of Li-Zn. Fig. 6c demonstrates the specific capacity at the varied current densities of 100 mA g⁻¹, 300 mA g⁻¹, 700 mA g⁻¹, 1000 mA g⁻¹, 1500 mA g⁻¹, and 2000 mA g⁻¹, respectively to verify the high-rate Li-ion storage performance of all the fabricated electrodes. As the applied current density is increased from 100 to 2000 mA g⁻¹, the specific capacity naturally decreases due to the insufficient kinetic properties including ion diffusivity and electrical conductivity compared with high current density. In this regard, ZnOS/SCNF electrode reports the highest specific capacity of 408.51 mAh g⁻¹ at a current density of 2000 mA g⁻¹ and the capacity retention rate of 62.1% compared to those of the CNF (126.37 mAh g⁻¹ with the retention rate of 45.3%), ZnO/CNF (249.68 mAh g⁻¹ with the retention rate of 43.5%), and ZnS/SCNF (306.09 mAh g⁻¹ with the retention rate of 59.2%). Moreover, ZnOS/SCNF electrodes exhibit superior reversibility of ~98% at the returned 100 mA g⁻¹ current density compared with the initial ten cycles. This remarkable rate capability of ZnOS/SCNF is ascribed to the efficient Li-ion transportation through the expanded ZnOS lattice constant and enhanced electrical conductivity at the interface of ZnO and ZnS. Fig. 6d represents the ultrafast cycling stability of all the fabricated electrodes at a high current density of 2000 mA g⁻¹, which is considered an important factor for practical applications. After an aging procedure of 10 cycles with 100 mA g⁻¹, long-term cycling performances were evaluated at a high current density of 2000 mA g⁻¹ up to 500 cycles. Compared with the CNF (129.7 mAh g⁻¹ after 500 cycles), ZnO/CNF (93.65 mAh g⁻¹ after 500 cycles), and ZnS/SCNF (197.89 mAh g⁻¹ after 500 cycles), ZnOS/SCNF shows an outstanding specific capacity of 347.02 mAh g⁻¹ with a capacity retention of 85.4% after 500 cycles at a current density of 2000 mA g⁻¹. As discussed in the EIS data, this superior ultrafast cycling capability is attributed to the enhanced charge transfer efficiency between ZnO and ZnS with S-doped CNF matrix and interfacial lattice distortion of ZnOS/SCNF, inducing the electrical conductivity enhancement and offering efficient Li-ion diffusion path.

To further investigate the electrochemical kinetic behavior, CV measurements of CNF and ZnOS/SCNF were performed at the

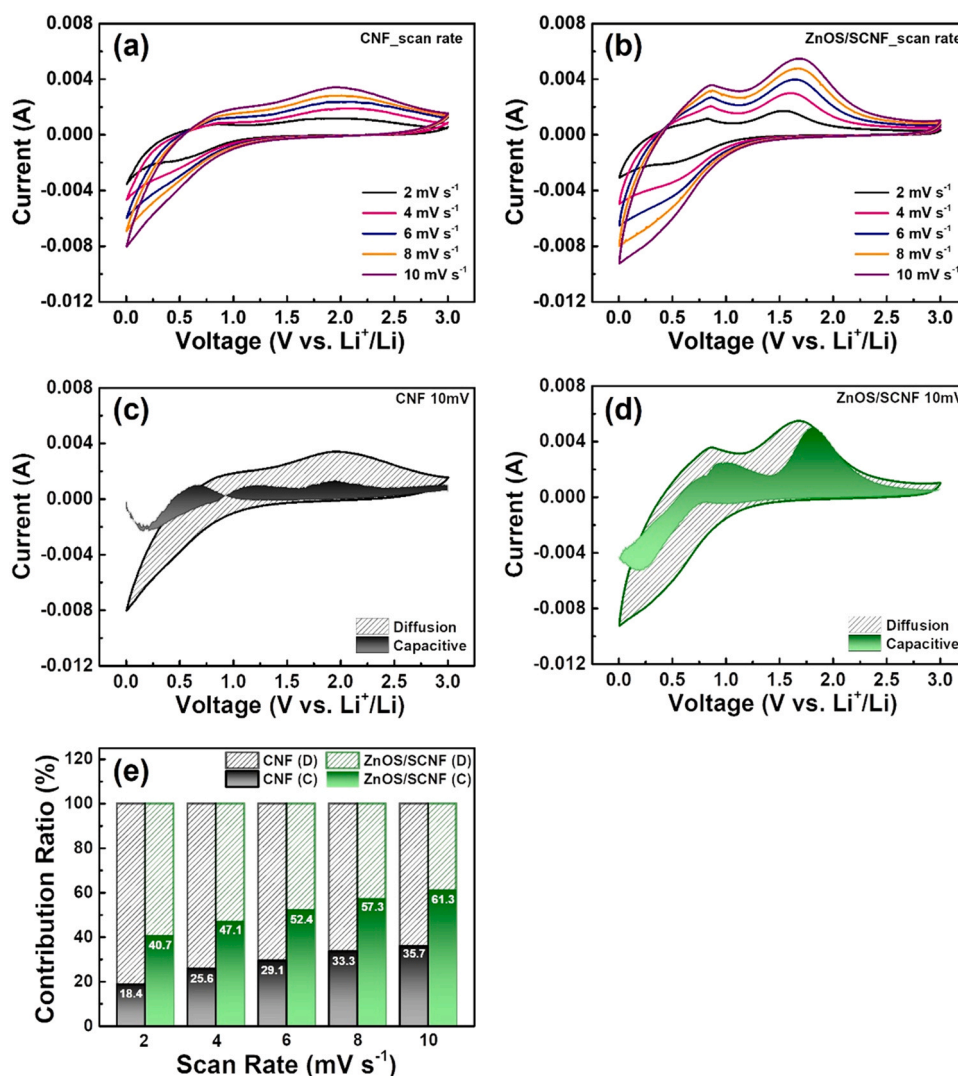


Fig. 7. (a, b) CV curves of CNF and ZnOS/SCNF with varied scan rate from 2 to 10 mV s⁻¹, (c, d) CV curves of CNF and ZnOS/SCNF, which are separated to diffusion current for shaded region and capacitive current for filled region at 10 mV s⁻¹, and (e) area comparison of diffusion (D) and capacitive (C) contributions for CNF and ZnOS/SCNF electrodes with different scan rates.

different scan rate from 2 mV s⁻¹ to 10 mV s⁻¹ (see Fig. 7a,b). Both CV curves of CNF and ZnOS/SCNF revealed increasing peak area by the scan rate increment, maintaining similar curve shapes. The capacitive proportion of the electrode during the charge/discharge reaction can be calculated via following equation (Eq. (5)) [39].

$$i(V) = k_1v + k_2v^{1/2} \quad (5)$$

in which k_1v and $k_2v^{1/2}$ correspond to the capacitive behavior and diffusion control region, respectively. Therefore, the CV curves of CNF and ZnOS/SCNF electrode can be divided into two parts as shown in Fig. 7c,d. The capacitive dominant CV curve indicates a rapid charge transfer with fast lithium ion diffusion, which can significantly affect to the ultrafast Li-ion storage capability [40]. Fig. 7e summarizes the capacitive proportion of the CNF with ZnOS/SCNF electrodes by the scan rate variation. Compared with the CNF and other samples (see Fig. S7), ZnOS/SCNF electrodes show the highest capacitive behavior ratio of 61.3% at a scan rate of 10 mV s⁻¹, which is in agreement with the excellent rate capability of ZnOS/SCNF, as shown in Fig. 6c.

This study suggests a novel hybrid structure of ZnOS lamination layer on S-doped CNF matrix and reveals its structural advantage as an anode material in detail. The ZnOS/SCNF electrode exhibited high specific capacity, cycling stability, and ultrafast Li-ion storage

capability, which are crucial parts for overcoming the limitation of LIB application. This remarkable performance enhancement can be attributed to the below factors. First, high electrical conductivity of ZnOS/SCNF was obtained through the enhanced charge transfer efficiency at the interface of ZnO and ZnS with S-doped CNF matrix, enabling superior ultrafast Li-ion storage capability. Second, generated Li₂O and Li₂S interphase during the conversion reaction of ZnOS can suppress the drastic alloying process of Zn, which realize the high cycle stability during repetitive charge/discharge process. Therefore, the hybrid ZnOS/SCNF electrode demonstrates great potential as a candidate for ultrafast LIB anode.

4. Conclusion

In summary, we successfully developed a hybrid structure of an ZnOS lamination layer on S-doped CNF matrix (ZnOS/SCNF) for an ultrafast and stable LIB anode using electrospinning method and sequential ALD process. Through the development of the ZnOS/SCNF hybrid structure, superior kinetic property of ZnOS and high electrical conductivity of S-doped CNF can be achieved. It should be noted that during the charge/discharge process of ZnOS, a highly reversible conversion and alloying reaction with Li-ion occurs. Moreover, the distorted lattice structure at the interfacial region of

ZnO/ZnS can facilitate the Li-ion transportation, resulting in the highest Li-ion diffusion coefficient of $9.14 \times 10^{-13} \text{ cm}^2 \text{ s}^{-1}$ for ZnOS/SCNF electrode. ZnOS/SCNF electrode showed competitive electrochemical performance such as high specific capacity of 672.8 mAh g^{-1} at 100 mA g^{-1} with great capacity retention of 87.8% after 100 cycles, superior high rate capacity of $408.51 \text{ mAh g}^{-1}$ at 2000 mA g^{-1} , and excellent ultrafast cycling stability of 85.4% after 500 cycles. The improvement of the electrochemical performance was attributed to the (1) enhanced electrical conductivity from the efficient charge transfer at the ZnO/ZnS interfaces and S-doped CNF matrix for the ultrafast Li-ion storage capability, and (2) generation of Li_2O and Li_2S interphase during the conversion and alloying process of ZnOS/SCNF anode for superior cycle stability. Thus, the suggested novel ZnOS/SCNF hybrid structure can be a effective strategy for achieving ultrafast and stable Li-ion storage performance for the anode material of LIBs.

CRedit authorship contribution statement

Kue-Ho Kim: Conceptualization, Methodology, Investigation, Data curation, Writing – original draft. **Weiguang Hu:** Conceptualization, Methodology, Data curation. **Hyo Sik Chang:** Conceptualization, Supervision, Writing – review & editing. **Hyo-Jin Ahn:** Conceptualization, Supervision, Writing – review & editing.

Acknowledgements

This study was supported by the Research Program funded by SeoulTech (Seoul National University of Science and Technology).

Declaration of Competing Interest

The authors declare that they have no known competing financial interests or personal relationships that could have appeared to influence the work reported in this paper.

Appendix A. Supporting information

Supplementary data associated with this article can be found in the online version at [doi:10.1016/j.jallcom.2021.163148](https://doi.org/10.1016/j.jallcom.2021.163148).

References

1. M. Armand, J.-M. Tarascon, Building better batteries, *Nature* 451 (2008) 652–657, <https://doi.org/10.1038/451652a>
2. B. Dunn, H. Kamath, J.-M. Tarascon, Electrical energy storage for the grid: a battery of choices, *Science* 334 (2011) 928–935, <https://doi.org/10.1126/science.1212741>
3. P. Santhoshkumar, T. Subburaj, A. Kathalingam, K. Karuppasamy, D. Vikraman, C.-J. Yim, H.-C. Park, H.-S. Kim, Potential core-shell anode material for rechargeable lithium-ion batteries: encapsulation of titanium oxide nanostructure in conductive polymer, *J. Alloy. Compd.* 882 (2021) 160715, <https://doi.org/10.1016/j.jallcom.2021.160715>
4. K.-W. Sung, D.-Y. Shin, H.-J. Ahn, Boosting ultrafast Li storage kinetics of conductive Nb-doped TiO_2 functional layer coated on LiMn_2O_4 , *J. Alloy. Compd.* 870 (2021) 159404, <https://doi.org/10.1016/j.jallcom.2021.159404>
5. C.-J. He, Y.-Q. Wang, W.-J. Meng, J. Zhang, Y. Xie, Y.-L. Hou, D.-L. Zhao, Hierarchical microspheres constructed by SnS_2 nanosheets and S-doped graphene for high performance lithium/sodium-ion batteries, *J. Alloy. Compd.* 889 (2021) 161648, <https://doi.org/10.1038/451652a>
6. X. Wu, S. Xia, Y. Huang, X. Hu, B. Yuan, S. Chen, Y. Yu, W. Liu, High-performance, low-cost, and dense-structure electrodes with high mass loading for lithium-ion batteries, *Adv. Funct. Mater.* 29 (2019) 1903961, <https://doi.org/10.1002/adfm.201903961>
7. C.P. Grey, D.S. Hall, Prospects for lithium-ion batteries and beyond—a 2030 vision, *Nat. Commun.* 11 (2020) 6279, <https://doi.org/10.1038/s41467-020-19991-4>
8. Z. Hu, X. Xu, X. Wang, K. Yu, C. Liang, Ultrafine SnO_2 nanoparticles anchored in the porous corn straw carbon substrate for high-performance Li-ion batteries application, *J. Alloy. Compd.* 835 (2020) 155446, <https://doi.org/10.1016/j.jallcom.2020.155446>
9. J.-G. Wang, H. Liu, H. Liu, Z. Fu, D. Nan, Facile synthesis of microsized MnO/C composites with high tap density as high performance anodes for Li-ion

- batteries, *Chem. Eng. J.* 328 (2017) 591–598, <https://doi.org/10.1016/j.cej.2017.07.039>
10. S. Guo, J. Liu, Q. Zhang, Y. Jin, H. Wang, Metal organic framework derived $\text{Co}_3\text{O}_4/\text{Co}/\text{NeC}$ composite as high-performance anode material for lithium-ion batteries, *J. Alloy. Compd.* 855 (2021) 157538, <https://doi.org/10.1016/j.jallcom.2020.157538>
11. Y. Li, Y. Huang, X. Wang, W. Liu, K. Yu, C. Liang, Simple synthesis of rice husk hollow carbon-coated flower ZnO for the anode in a high performance lithium-ion battery, *J. Phys. Chem. Solids* 145 (2020) 109540, <https://doi.org/10.1016/j.jpcs.2020.109540>
12. D.-Y. Shin, J.S. Lee, B.-R. Koo, H.-J. Ahn, Hierarchical hybrid nanostructure of 1T-tungsten disulfide quantum dots/multihollow capillary bundle-type mesoporous carbon for ultrafast and ultrastable lithium storage, *Chem. Eng. J.* 412 (2021) 128547, <https://doi.org/10.1016/j.cej.2021.128547>
13. W. Zhang, Z. Huang, H. Zhou, S. Li, C. Wang, H. Li, Z. Yan, F. Wang, Y. Kuang, Facile synthesis of ZnS nanoparticles decorated on defective CNTs with excellent performances for lithium-ion batteries anode material, *J. Alloy. Compd.* 816 (2020) 152633, <https://doi.org/10.1016/j.jallcom.2019.152633>
14. B. Zhao, D. Song, Y. Ding, J. Wu, Z. Wang, Z. Chen, Y. Jiang, J. Zhang, Ultrastable Li-ion battery anodes by encapsulating SnS nanoparticles in sulfur-doped graphene bubble films, *Nanoscale* 12 (2020) 3941–3949, <https://doi.org/10.1039/c9nr10608a>
15. H. Li, Y. Wei, Y. Zhang, F. Yin, C. Zhang, G. Wang, Z. Bakenov, Synthesis and electrochemical investigation of highly dispersed ZnO nanoparticles as anode material for lithium-ion batteries, *Ionics* 22 (2016) 1387–1393, <https://doi.org/10.1007/s11581-016-1661-x>
16. B.-R. Koo, K.-W. Sung, Boosting ultrafast lithium storage capability of hierarchical core/shell constructed carbon nanofiber/3D interconnected hybrid network with nanocarbon and FTO nanoparticle heterostructures, *Adv. Funct. Mater.* 30 (2020) 2001863, <https://doi.org/10.1002/adfm.202001863>
17. X. Huang, M.-G. Willinger, H. Fan, Z.-L. Xie, L. Wang, A. Klein-Hoffmann, F. Girgsdies, C.-S. Lee, X.-M. Meng, Single crystalline wurtzite ZnO/zinc blende ZnS coaxial heterojunctions and hollow zinc blende ZnS nanotubes: synthesis, structural characterization and optical properties, *Nanoscale* 6 (2014) 8787–8795, <https://doi.org/10.1039/c4nr01575d>
18. H. Xu, Y.-N. Zhou, F. Lu, Z.-W. Fu, Electrochemistry of $\text{ZnO}_{1-x}\text{S}_x$ thin film with lithium, *J. Electrochem. Soc.* 158 (2011) A285–A290, <https://doi.org/10.1149/1.3532037>
19. J. Song, H. Kim, W. Jae, T. Kim, C.M. Futralan, J. Kim, Porous ZnO/C microspheres prepared with maleopimaric acid as an anode material for lithium-ion batteries, *Carbon* 165 (2020) 55–66, <https://doi.org/10.1016/j.carbon.2020.04.035>
20. B. Tian, H. Xiang, L. Zhang, Z. Li, H. Wang, Niobium doped lithium titanate as a high rate anode material for Li-ion batteries, *Electrochim. Acta* 55 (2010) 5453–5458, <https://doi.org/10.1016/j.electacta.2010.04.068>
21. D. Jiang, L. Cao, W. Liu, G. Su, H. Qu, Y. Sun, B. Dong, Synthesis and luminescence properties of Core/Shell ZnS:Mn/ZnO nanoparticles, *Nanoscale Res. Lett.* 4 (2009) 78–83, <https://doi.org/10.1007/s11671-008-9205-6>
22. W.-X. Mao, W. Zhang, Z.-X. Chi, R.-W. Lu, A.-M. Cao, L.-J. Wan, Core-shell structured $\text{Ce}_2\text{S}_3/\text{ZnO}$ and their potential as pigment, *J. Mater. Chem. A* 3 (2015) 2176–2180, <https://doi.org/10.1039/c4ta05797j>
23. A. Torabi, V.N. Staroverov, Band gap reduction in ZnO and ZnS by creating layered ZnO/ZnS heterostructures, *J. Phys. Chem. Lett.* 6 (2015) 2075–2080, <https://doi.org/10.1021/acs.jpcclett.5b00687>
24. B. Zhao, F. Mattelaer, J. Kint, A. Werbrout, L. Henderick, M. Minjauw, J. Dendooven, C. Detavernier, Atomic layer deposition of ZnO-SnO₂ composite thin film: the influence of structure, composition and crystallinity on lithium-ion battery performance, *Electrochim. Acta* 320 (2019) 134604, <https://doi.org/10.1016/j.electacta.2019.134604>
25. K.-H. Kim, J.-Y. Kim, H.-J. Ahn, Hetero-shaped mesoporous structure of carbon nanofibers for high-performance electrical double layer capacitors, *J. Ceram. Process. Res.* 22 (2021) 1–7, <https://doi.org/10.36410/jcpr.2021.22.3.1>
26. J. Zhang, T. Tan, Y. Zhao, N. Liu, Preparation of ZnO nanorods/graphene composite anodes for high-performance lithium-ion batteries, *Nanomaterials* 8 (2018) 966, <https://doi.org/10.3390/nano8120966>
27. M. Mao, L. Jiang, L. Wu, M. Zhang, T. Wang, The structure control of ZnS/graphene composites and their excellent properties for lithium-ion batteries, *J. Mater. Chem. A* 3 (2015) 13384–13389, <https://doi.org/10.1039/c5ta01501d>
28. S. Sinha, H.V. Ramasamy, D.K. Nandi, P.N. Didwal, J.Y. Cho, C.-J. Park, Y.-S. Lee, S.-H. Kim, J. Heo, Atomic layer deposited zinc oxysulfide anodes in Li-ion batteries: an efficient solution for electrochemical instability and low conductivity, *J. Mater. Chem. A* 6 (2018) 16515–16528, <https://doi.org/10.1039/c8ta04129f>
29. B. Liu, X. Hu, X. Li, Y. Li, C. Chen, K.-H. Lam, Preparation of ZnS@In₂S₃ core@shell composite for enhanced photocatalytic degradation of gaseous o-dichlorobenzene under visible light, *Sci. Rep.* 7 (2017) 16396, <https://doi.org/10.1038/s41598-017-16732-4>
30. R.R. Thankalekshmi, A.C. Rastogi, Structure and optical band gap of $\text{ZnO}_{1-x}\text{S}_x$ thin films synthesized by chemical spray pyrolysis for application in solar cells, *J. Appl. Phys.* 112 (2012) 063708, <https://doi.org/10.1063/1.4754014>
31. N. Galland, F. Caralp, M.-T. Rayez, Y. Hannachi, J.-C. Loison, G. Dorthé, A. Bergeat, Reaction of carbon atoms, $\text{C}(2p^2,^3P)$, with hydrogen sulfide, $\text{H}_2\text{S}(X^1A_1)$: overall rate constant and product channels, *J. Phys. Chem. A* 105 (2001) 9893–9900, <https://doi.org/10.1021/jp011713m>
32. K.-H. Kim, S.-J. Jeong, B.-R. Koo, H.-J. Ahn, Surface amending effect of N-doped carbon-embedded NiO films for multirole electrochromic energy-storage devices, *Appl. Surf. Sci.* 537 (2021) 147902, <https://doi.org/10.1016/j.apsusc.2020.147902>

- [33] D.-Y. Shin, H.-J. Ahn, Interfacial engineering of a heteroatom-doped graphene layer on patterned aluminum foil for ultrafast lithium storage kinetics, *ACS Appl. Mater. Interfaces* 12 (2020) 19210–19217, <https://doi.org/10.1021/acsami.0c01774>
- [34] G.-H. An, H. Kim, H.-J. Ahn, Improved ionic diffusion through the mesoporous carbon skin on silicon nanoparticles embedded in carbon for ultrafast lithium storage, *ACS Appl. Mater. Interfaces* 10 (2018) 6235–6244, <https://doi.org/10.1021/acsami.7b15950>
- [35] G.-H. An, D.-Y. Lee, H.-J. Ahn, Vanadium nitride encapsulated carbon fibre networks with furrowed porous surfaces for ultrafast asymmetric supercapacitors with robust cycle life, *J. Mater. Chem. A* 5 (2017) 19714–19720, <https://doi.org/10.1039/c7ta06345h>
- [36] S. Sinha, P.N. Didwal, D.K. Nandi, R. Verma, J.Y. Cho, S.-H. Kim, C.-J. Park, J. Heo, Revealing the simultaneous effects of conductivity and amorphous nature of atomic-layer-deposited double-anion-based zinc oxysulfide as superior anodes in Na-ion batteries, *Small* 15 (2019) 1900595, <https://doi.org/10.1002/sml.201900595>
- [37] H. Li, J. Wang, Y. Zhao, T. Tan, Synthesis of the ZnO@ZnS nanorod for lithium-ion batteries, *Energies* 11 (2018) 2117, <https://doi.org/10.3390/en11082117>
- [38] Y. Guo, Z. Wang, X. Lu, J. Lu, K. Rabia, H. Chen, R. Hu, H. Tang, Q. Zhang, Z. Li, Core-shell ZnO@C:N hybrids derived from MOFs as long-cycling anodes for lithium ion batteries, *Chem. Commun.* 56 (2020) 1980–1983, <https://doi.org/10.1039/c9cc08478a>
- [39] S.H. Lim, G.D. Park, Y.C. Kang, Investigation of cobalt hydroxysulfide as a new anode material for Li-ion batteries and its conversion reaction mechanism with Li-ions, *Chem. Eng. J.* 401 (2020) 126121, <https://doi.org/10.1016/j.cej.2020.126121>
- [40] L. Ao, C. Wu, Y. Xu, X. Wang, K. Jiang, L. Shang, Y. Li, J. Zhang, Z. Hu, J. Chu, A novel Sn particles coated composite of SnO_x/ZnO and N-doped carbon nanofibers as high-capacity and cycle-stable anode for lithiumion batteries, *J. Alloy. Compd.* 819 (2020) 153036, <https://doi.org/10.1016/j.jallcom.2019.153036>